

Doubly Charmed Tetraquark T_{cc}^+ from Lattice QCD near Physical Point

Yan Lyu,^{1,2,*} Sinya Aoki,^{3,2,†} Takumi Doi,^{2,‡} Tetsuo Hatsuda,^{2,§} Yoichi Ikeda,^{4,¶} and Jie Meng^{1,5,**}

¹State Key Laboratory of Nuclear Physics and Technology,
School of Physics, Peking University, Beijing 100871, China

²Interdisciplinary Theoretical and Mathematical Sciences Program (iTHEMS), RIKEN, Wako 351-0198, Japan

³Center for Gravitational Physics, Yukawa Institute for Theoretical Physics, Kyoto University, Kyoto 606-8502, Japan

⁴Center for Infectious Disease Education and Research, Osaka University, Suita 565-0871, Japan

⁵Yukawa Institute for Theoretical Physics, Kyoto University, Kyoto 606-8502, Japan

(Dated: October 18, 2023)

The doubly charmed tetraquark T_{cc}^+ recently discovered by the LHCb Collaboration is studied on the basis of $(2+1)$ -flavor lattice QCD simulations of the D^*D system with nearly physical pion mass $m_\pi = 146$ MeV. The interaction of D^*D in the isoscalar and S -wave channel, derived from the hadronic spacetime correlation by the HAL QCD method, is attractive for all distances and leads to a near-threshold virtual state with a pole position $E_{\text{pole}} = -59^{(+53)}_{(-99)} \text{ }^{(+2)}_{(-67)} \text{ keV}$ and a large scattering length $1/a_0 = 0.05(5)^{(+2)}_{(-2)} \text{ fm}^{-1}$. The virtual state is shown to evolve into a loosely bound state as m_π decreases to its physical value by using a potential modified to $m_\pi = 135$ MeV based on the pion-exchange interaction. Such a potential is found to give a semiquantitative description of the LHCb data on the $D^0D^0\pi^+$ mass spectrum. Future study is necessary to perform physical-point simulations with the isospin-breaking and open three-body-channel effects taken into account.

Introduction.— The quest of exotic hadrons with multi-quark configuration beyond the conventional constituent quark model has been one of central subjects in the study of nonperturbative QCD for decades [1–6]. Although dozens of candidates of exotic hadrons were reported [7, 8], a doubly charmed tetraquark T_{cc}^+ was discovered only recently by the LHCb Collaboration [9]: A pronounced narrow peak appears in the $D^0D^0\pi^+$ mass spectrum just around 360 keV below the $D^{*+}D^0$ threshold, and its isospin I , spin J , and parity P are found to be consistent with $(I, J^P) = (0, 1^+)$ [10].

Although early theoretical predictions on the mass of T_{cc}^+ were scattered in the range of ± 300 MeV with respect to the $D^{*+}D^0$ threshold, the constraint from the LHCb data starts to lead a consistent description on the basic properties of T_{cc}^+ in recent phenomenological models (see Refs. [11–22], and references therein). Nevertheless, a solid theoretical validation on the existence of T_{cc}^+ needs to be given from first-principles lattice QCD simulations. So far, the lattice QCD studies on the doubly charmed tetraquark in terms of the D^*D scattering length [23–25] and the finite-volume D^*D energy [26, 27] have been limited in the region of large pion masses ($m_\pi \geq 280$ MeV) and small lattice sizes ($L \leq 2.9$ fm).

Under the above circumstances, the purpose of this Letter is twofold. The first purpose is to report an investigation of the D^*D scattering in the $I = 0$ and S -wave channel from lattice QCD simulations with nearly physical pion mass $m_\pi = 146$ MeV and a large lattice size $L = 8.1$ fm. We employ the HAL QCD method [28–30] for converting the hadronic spacetime correlation to the physical observables. Shown in Fig. 1 is a summary of the previous lattice QCD calculations of the inverse scat-

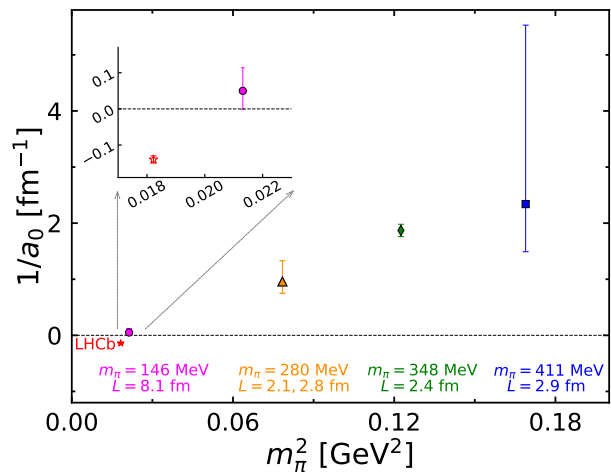


FIG. 1. The inverse of scattering length $1/a_0$ for the D^*D scattering in the $I = 0$ and S -wave channel obtained from lattice QCD simulations by Refs. [23](blue square), [24](green diamond), and [25](yellow triangle). The result of the present Letter (magenta circle) and the real part of the experimental value by LHCb (red star) [10] are also shown.

tering length of D^*D as a function of m_π^2 . The recent LHCb result and the result of the present Letter are also shown. Figure 1 indicates a clear trend that the lattice data approach the experimental data as the pion mass decreases toward the physical point. Our second purpose is to make a direct comparison between theoretical and experimental $D^0D^0\pi^+$ mass spectra to unveil the properties of near-threshold tetraquark. The HAL QCD method is best suited for such comprehensive analysis, since it provides the D^*D scattering T matrix and al-

lows us to study how the mass spectrum changes toward the physical point.

HAL QCD method.— The starting point for deriving D^*D interaction in the HAL QCD method is the normalized spacetime correlation [28–30],

$$\begin{aligned} R(\mathbf{r}, t) &= \sum_{\mathbf{x}} \langle 0 | D^*(\mathbf{x} + \mathbf{r}, t) D(\mathbf{x}, t) \bar{\mathcal{J}}(0) | 0 \rangle / e^{-(m_{D^*} + m_D)t} \\ &= \sum_n A_n \psi_n(\mathbf{r}) e^{-(\Delta E_n)t} + O(e^{-(\Delta E^*)t}), \end{aligned} \quad (1)$$

where $\Delta E_n = \sqrt{m_{D^*} + \mathbf{k}_n^2} + \sqrt{m_D + \mathbf{k}_n^2} - (m_{D^*} + m_D)$ with \mathbf{k}_n being relative momentum in the center-of-mass frame. The equal-time Nambu-Bethe-Salpeter wave function for each elastic scattering state is defined as $\psi_n(\mathbf{r})$, and the coupling strength to the n th eigenstate is denoted by $A_n = \langle E_n | \bar{\mathcal{J}}(0) | 0 \rangle$. We use local sink operators of the form $\bar{q}(x)\Gamma c(x)$ with $\Gamma = \gamma_i$ (γ_5) for D^* (D), where $q(x)$ denotes either $u(x)$ or $d(x)$. For the source, the wall-type operator \mathcal{J} at $t = 0$, defined by replacing $q(\mathbf{x}, t)$ with $\sum_{\mathbf{x}} q(\mathbf{x}, t)$ and $c(\mathbf{x}, t)$ with $\sum_{\mathbf{x}} c(\mathbf{x}, t)$, is adopted together with the Coulomb gauge fixing. Although the wall-type source may have weak coupling to compact states, it is a suitable operator for studying near-threshold and loosely bound T_{cc}^+ . By projecting into quark zero momentum mode, such a source operator is expected to have large overlap with the low-energy D^*D scattering states. The lowest relevant (noninteracting) energy levels of three-body inelastic state ($DD\pi$) and two-body inelastic state (D^*D^*) are $\Delta E^* \simeq \sqrt{m_D^2 + (2\pi/L)^2} + \sqrt{m_\pi^2 + (2\pi/L)^2} - m_{D^*} = 78$ MeV and $\Delta E^* \simeq m_{D^*} - m_D = 140$ MeV, respectively. They are suppressed by the combination of the small overlap with our wall-type source operator and the factor $e^{-(\Delta E^*)t}$. The S -wave projection of $R(\mathbf{r}, t)$ on the lattice is carried out by the Misner method [31]. A comparison between S - and D - wave components of $R(\mathbf{r}, t)$ is given in Fig. S1 in [32], and we find the D -wave component is highly suppressed to only $\lesssim O(0.1)\%$, similar to the observations in Refs. [18, 25].

The correlation function $R(\mathbf{r}, t)$ is known to satisfy the partial differential equation [29, 33],

$$\begin{aligned} \left[\frac{1 + 3\delta^2}{8\mu} \partial_t^2 - \partial_t - H_0 + O(\delta^2 \partial_t^3) \right] R(\mathbf{r}, t) \\ = \int d\mathbf{r}' U(\mathbf{r}, \mathbf{r}') R(\mathbf{r}', t), \end{aligned} \quad (2)$$

where $H_0 = \frac{-\nabla^2}{2\mu}$, $\mu = \frac{m_{D^*} m_D}{m_{D^*} + m_D}$, $\delta = \frac{m_{D^*} - m_D}{m_{D^*} + m_D}$. The integral kernel $U(\mathbf{r}, \mathbf{r}')$ is defined through $[\mathbf{k}_n^2/(2\mu) - H_0]\psi_n(\mathbf{r}) = \int d\mathbf{r}' U(\mathbf{r}, \mathbf{r}') \psi_n(\mathbf{r}')$. The $O(\delta^2 \partial_t^3)$ term is found to be consistent with zero within statistical error and is neglected in our analysis. The derivative expansion $U(\mathbf{r}, \mathbf{r}') = \sum_n V_n(\mathbf{r}) \nabla^n \delta(\mathbf{r} - \mathbf{r}')$ at the leading order gives an effective local potential,

$$V(r) = R^{-1}(\mathbf{r}, t) \left[\frac{1 + 3\delta^2}{8\mu} \partial_t^2 - \partial_t - H_0 \right] R(\mathbf{r}, t). \quad (3)$$

The truncation error from higher-order terms of the derivative expansion can be estimated through the t dependence of $V(r)$ [29, 34, 35]. Once the potential is obtained, it can be used to calculate physical quantities by solving the stationary Schrödinger equation, $[H_0 + V(r)]\psi(\mathbf{r}) = E\psi(\mathbf{r})$, in the infinite spatial volume.

Lattice setup.— The $(2+1)$ -flavor gauge configurations are generated on the 96^4 lattice with the Iwasaki gauge action and the nonperturbatively $O(a)$ -improved Wilson quark action at nearly physical point ($m_\pi = 146.4$ MeV) [36]. The lattice spacing is $a = 0.0846$ fm, corresponding to lattice size $L = 8.1$ fm. For the charm quark, the relativistic heavy quark (RHQ) action is employed in order to remove the cutoff errors associated with the charm quark mass up to next-to-next-to-leading order [37]. The charm quark mass is set to be very close to its physical value, which leads to a spin-averaged $1S$ charmonium mass $M_{\text{av}} \equiv (m_{\eta_c} + 3m_{J/\psi})/4 = 3096.6$ MeV, 0.9% larger than the physical value [38]. By comparing results from another set of RHQ parameters corresponding to $M_{\text{av}} = 3051.4$ MeV, 0.6% smaller than the physical value, we confirm that effect from slightly unphysical charm quark is small compared with current statistical uncertainties.

With 200 gauge configurations, we perform 640 measurements ($= 4$ directions $\times 80$ source positions $\times 2$ forward-backward propagations) [39] for each configuration to increase the statistics. The jackknife method and bootstrap method are used to estimate the statistical error with a bin size of 20 configurations throughout this Letter; a comparison with a bin size of 40 shows that the bin size dependence is small. The quark propagators are calculated by the domain-decomposed solver [40] and the Bridge++ code [41] with the periodic boundary condition for all directions. The unified contraction algorithm is used to obtain the hadronic correlation functions [42]. The D^* and D masses from the correlated single-state fit in the temporal region $t/a = 20 - 30$ are $m_{D^*} = 2018.1(5)$ MeV and $m_D = 1878.2(2)$ MeV with statistical error shown in the parenthesis, which are 0.5% heavier than the physical values. (For the effective mass plots, see Fig. S2 in [32].) With our slightly heavy pion mass, m_{D^*} is below the $D\pi$ threshold, so that D^* is stable against the strong decay. Other systematic errors can be estimated as follows: (i) The finite cutoff effect is $O[(a\Lambda_{\text{QCD}})^2, \alpha_s^2 a\Lambda_{\text{QCD}}] \simeq O(1)\%$ thanks to $O(a)$ improvement for the light quarks and RHQ action for the charm quark, (ii) the finite volume effect is as small as $\exp[-m_h(L/2)] \simeq 0.3\%$ (where $m_h = 2m_\pi$ as described below) thanks to the large volume, and (iii) the quenched charm quark effect is expected to be highly suppressed by the heavy charm quark mass [43].

Interaction potential.— We show in Fig. 2 the D^*D potential $V(r)$ in the $I = 0$ and S -wave channel defined in Eq. (3) for $t/a = 21, 22$, and 23, corresponding to $t \simeq 1.9$ fm. This temporal region is chosen to suppress inelastic

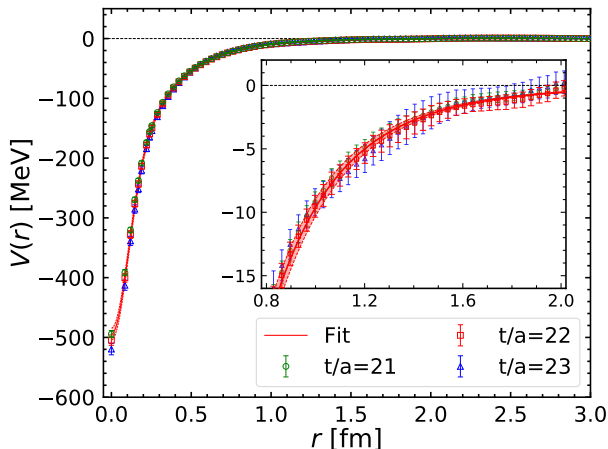


FIG. 2. The D^*D potential $V(r)$ in the $I = 0$ and S -wave channel at Euclidean time $t/a = 21$ (green circles), 22 (red squares), and 23 (blue triangles). The red band shows the fitted potential with V_{fit}^B for $t/a = 22$. The inset shows a magnification.

states contamination at smaller t and simultaneously to avoid large statistical errors at larger t . A small variation of the potentials for different t/a is observed and is taken into account as a source of the systematic error.

For later convenience, we perform a correlated fit to the potential in Fig. 2 in the range $0 < r < 2$ fm by a phenomenological four-range Gaussian, $V_{\text{fit}}^A(r) = \sum_{i=1}^4 a_i e^{-(r/b_i)^2}$. Fitting parameters at $t/a = 22$ are $(a_1, a_2, a_3, a_4) = [-269(6), -121(10), -81(12), -23(14)]$ in MeV and $(b_1, b_2, b_3, b_4) = [0.14(1), 0.27(1), 0.52(5), 0.97(16)]$ in fm with an accuracy of $\chi^2/\text{d.o.f.} = 1.01$. The fitted potential is shown in Fig. S3 in [32] with the normalized covariance matrix of the fitted parameters given in Eq.(S2) in [32].

The D^*D potential in the $(I, J^P) = (0, 1^+)$ channel shown in Fig. 2 is attractive for all distances. This is consistent with the result previously found for heavy pion masses [23]: The short-range attraction was suggested to be related to the attractive (anti)diquark configuration $(\bar{u}\bar{d})_{\mathbf{3}_s, I=J=0} - (cc)_{\mathbf{3}_s^*, J=1}$, coupled to the asymptotic D^*D state [44–48] (for an interpretation based on the string model, see Ref. [49]). Similar short-range attraction was also found for the B^*B system in the $(I, J^P) = (0, 1^+)$ channel [50, 51]. The long-range part of the attraction for $r > 1$ fm would have contributions from the one-pion exchange (OPE) between D^* and D of the form $\sim e^{-m_\pi r}/r$ with either $m = m_\pi$ [52] or $m = \sqrt{(m_{D^*} - m_D)^2 - m_\pi^2}$ [53], and from the two-pion exchange (TPE) of the form $\sim (e^{-m_\pi r}/r)^2$ [39].

To study different possibilities for the long-range part, we introduce the following fit function with the Gaussian-

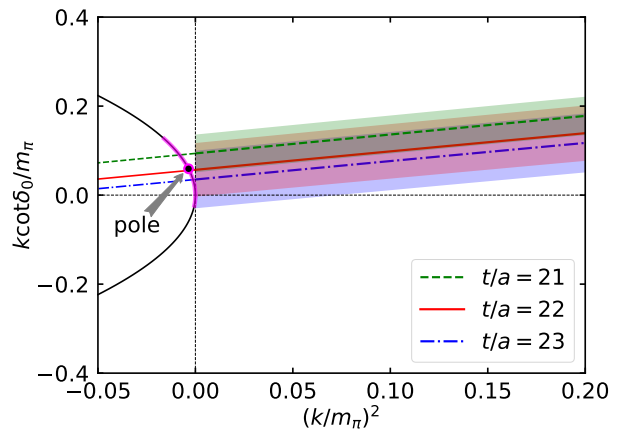


FIG. 3. The $k \cot \delta_0/m_\pi$ for D^*D scattering in the $I = 0$ and S -wave channel as a function of $(k/m_\pi)^2$. The intersection of $k \cot \delta_0/m_\pi$ and the black solid line $[\pm\sqrt{-(k/m_\pi)^2}]$ denotes the pole of the scattering amplitude. The pole position is shown by the black point with magenta line indicating statistical and systematic errors combined.

type form factor [39]:

$$V_{\text{fit}}^B(r; m_\pi) = \sum_{i=1,2} a_i e^{-(r/b_i)^2} + a_3 \left(1 - e^{-(r/b_3)^2}\right)^n V_\pi^n(r) \quad (4)$$

with $V_\pi(r) = e^{-m_\pi r}/r$. We find that $n = 2$ and $m_\pi = 146.4$ MeV provide a best fit with the parameter set, $(a_1, a_2) = [-276(6), -219(8)]$ in MeV, $a_3 = -43(3)$ MeV·fm², and $(b_1, b_2, b_3) = [0.14(1), 0.28(1), 0.43(2)]$ in fm, with an accuracy of $\chi^2/\text{d.o.f.} = 0.96$. The fitted potential is shown by the red band in Fig. 2. Also, we find that neither $n = 1$ and $m_\pi = 146.4$ MeV nor $n = 1$ and $m_\pi \rightarrow \sqrt{(m_{D^*} - m_D)^2 - m_\pi^2}$ can reproduce the long-range part of the potential. In Fig. S4 in [32], the spatial effective energy $E_{\text{eff}}(r) = -\frac{\ln[V(r)r^2/a_3]}{r}$ with the lattice data for $V(r)$ and a_3 as inputs is shown to have a plateau at $2m_\pi = 292.8$ MeV for $1 < r < 2$ fm. This indicates that the long-range part is consistent with the TPE. It is an open question why the theoretically possible OPE contribution does not appear in the lattice data.

Scattering parameters and pole position.— Using the potential fitted to our lattice data, we calculate the S -wave scattering phase shifts δ_0 by solving the Schrödinger equation in the infinite spatial volume with $m_{D^{(*)}}$ measured on the lattice. Figure 3 shows the $k \cot \delta_0/m_\pi$ as a function of $(k/m_\pi)^2$ with k being a relative momentum. The scattering length a_0 and the effective range r_{eff} are obtained by an effective-range expansion (with the sign convention of high-energy physics) as

$$k \cot \delta_0 = \frac{1}{a_0} + \frac{1}{2} r_{\text{eff}} k^2 + O(k^4), \quad (5)$$

and are given in the second column of Table I. The central

values and the statistical errors in the first parentheses are obtained at $t/a = 22$ with V_{fit}^B , while the systematic errors in the second parentheses are obtained by comparing results from different $t/a = 21 - 23$ with $V_{\text{fit}}^{A,B}$.

The scattering length obtained in this way is shown by the magenta circle in Fig. 1 together with the previous lattice results and the LHCb experimental data. As mentioned in the *Introduction*, there is a clear tendency that $1/a_0$ from lattice data approaches the unitary regime ($1/a_0 \sim 0$) as the pion mass decreases. Also, our result at $m_\pi = 146.4$ MeV produces a virtual state, which implies that a marginal modification of the interaction (e.g. by reducing the quark mass) may bring such a near-threshold virtual state to a loosely bound state. A typical example of virtual or bound state sensitive to the quark mass is dineutron or deuteron in nuclear physics [54–56]. A bound (virtual) state is characterized by a pole of the scattering amplitude $f(k)$ on the positive (negative) side of the imaginary axis at $k = i\kappa_{\text{pole}}$. Since $f^{-1}(k)$ is proportional to $k \cot \delta_0$, virtual and bound poles near threshold can be inferred from the intersection between $\frac{1}{a_0} + \frac{1}{2}r_{\text{eff}}k^2$ and $\pm\sqrt{-k^2}$. As shown in Fig. 3, we indeed find a near-threshold virtual state pole. The actual value of the pole position in the complex k plane for the present pion mass is shown in the second column of Table I, together with the pole energy, $E_{\text{pole}} = \sqrt{m_{D^*}^2 - \kappa_{\text{pole}}^2} + \sqrt{m_D^2 - \kappa_{\text{pole}}^2} - (m_{D^*} + m_D)$. We confirm that κ_{pole} and E_{pole} here have numerically the same values with those directly obtained from the T matrix, indicating that the left-hand cut associated with TPE is negligible. The effect on E_{pole} from slightly unphysical charm quark mass is found to be about -30 keV, smaller than statistical and systematic errors in Table I.

To estimate how the scattering parameters change and the pole evolves toward the physical point, we modify the potential by taking $m_\pi = 135.0$ MeV (approximately the physical pion mass without the QED contribution [57]) with the other parameters ($a_{1,2,3}, b_{1,2,3}$) of V_{fit}^B at $t/a = 22$ kept fixed. Using such a potential together with physical m_{D^*,D^0} [58] we find a loosely

TABLE I. Results for $1/a_0$, the effective range r_{eff} , the pole position κ_{pole} , and E_{pole} . Numbers in the second column with statistical error (first parentheses) and systematic error (second parentheses) are obtained from $V_{\text{fit}}^{A,B}(r)$ with $t/a = 21 - 23$ at $m_\pi = 146.4$ MeV. The third column shows estimated values from $V_{\text{fit}}^B(r; m_\pi)$ with $t/a = 22$ and $m_\pi = 135.0$ MeV. The asymmetric statistical error for E_{pole} is due to its non-normal distribution (see Fig. S5 in [32]).

m_π (MeV)	146.4	135.0
$1/a_0$ (fm^{-1})	0.05(5) $\left(\begin{smallmatrix} +2 \\ -2 \end{smallmatrix}\right)$	-0.03(4)
r_{eff} (fm)	1.12(3) $\left(\begin{smallmatrix} +3 \\ -8 \end{smallmatrix}\right)$	1.12(3)
κ_{pole} (MeV)	-8(8) $\left(\begin{smallmatrix} +3 \\ -5 \end{smallmatrix}\right)$	+5(8)
E_{pole} (keV)	-59 $\left(\begin{smallmatrix} +53 \\ -99 \end{smallmatrix}\right)$ $\left(\begin{smallmatrix} +2 \\ -67 \end{smallmatrix}\right)$	-45 $\left(\begin{smallmatrix} +41 \\ -78 \end{smallmatrix}\right)$

bound state with the scattering parameters and pole positions given in the third column of Table I. This indicates the existence of a bound T_{cc}^+ at physical point, though there is still a quantitative difference from the experimental value $E_{\text{pole}} = -360(40) \left(\begin{smallmatrix} +4 \\ -0 \end{smallmatrix}\right)$ keV reported by LHCb Collaboration [10]. Since the above estimate does not account for the isospin-breaking effect nor the open three-body-channel effect, future works should directly perform $(1+1+1)$ -flavor or $(1+1+1+1)$ -flavor lattice QCD + QED simulations with physical quark masses and the three-body channels ($D^0 D^0 \pi^+$ and $D^0 D^+ \pi^0$) considered.

Let us make an alternative estimate of a_0 at the physical point by taking the present and previous lattice data shown in Fig. 1 (note that these data are from different calculations and possess different lattice systematics): By using the simplest fit function $1/a_0(m_\pi) = c + dm_\pi^2$, we find $1/a_0 = -0.01(9) \text{ fm}^{-1}$ for $m_\pi = 135.0$ MeV (Fig. S6 in [32]). This result is consistent with $1/a_0 = -0.03(4) \text{ fm}^{-1}$ obtained by V_{fit}^B with the same pion mass in Table I, supporting the validity of our modification procedure for V_{fit}^B .

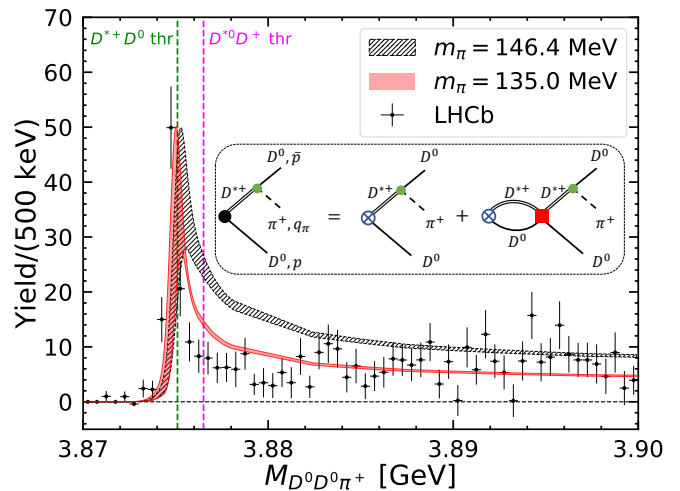


FIG. 4. The $D^0 D^0 \pi^+$ mass spectrum. Theoretical results with $V_{\text{fit}}^B(r; m_\pi)$ for $m_\pi = 146.4$ MeV ($m_\pi = 135.0$ MeV) are shown by the black (red) band. The black points are LHCb data [10]. The inset shows diagrams contributing to the $D^0 D^0 \pi^+$ mass spectrum, where the black filled circle, blue cross circle, green filled circle, and red square denote production amplitude U , constant vertex P , $D^{*+} \rightarrow D^0 \pi^+$ vertex, and scattering T matrix, respectively.

$D^0 D^0 \pi^+$ mass spectrum.— In order to make a further connection to the LHCb experimental data, let us now construct $D^0 D^0 \pi^+$ mass spectrum based on the above interaction by considering the rescattering between D^{*+} and D^0 along the line with Refs. [18, 59]. Within a single channel framework, we first construct a production amplitude $U(M, p)$ for $D^{*+} D^0$ pair with invariant mass M and relative momentum p in the $I = 0$ and S -wave

channel generated from a constant vertex P . Then the amplitude consisting of a direct production process and a rescattering process is written as (see the inset in Fig. 4),

$$U(M, p) = P + \int \frac{d^3\mathbf{q}}{(2\pi)^3} T(M, p, q) G(M, q) P. \quad (6)$$

Here the T matrix $T(M, p, q)$ with incoming (outgoing) momentum q (p) is obtained by solving the Lippmann-Schwinger equation with a given potential. The $D^{*+}D^0$ propagator is denoted as $G(M, q) = \left(M - m_{D^{*+}} - m_{D^0} - \frac{q^2}{2\mu} + \frac{i}{2}\Gamma_{D^{*+}}\right)^{-1}$ where $\Gamma_{D^{*+}} = 82.5$ keV is the decay width of D^{*+} [58], representing the unstable nature of D^{*+} in the real world. We set $P = 1$ without loss of generality, since it can be absorbed into an overall normalization factor. Then, the $D^0D^0\pi^+$ mass spectrum reads

$$\frac{d\text{Br}[D^0D^0\pi^+]}{dM} = \mathcal{N} \int dpd\bar{p} \int \bar{p}d\bar{\bar{p}} |U(M, p)G(M, p)q_\pi(p) + U(M, \bar{p})G(M, \bar{p})q_\pi(\bar{p})|^2, \quad (7)$$

where the pion momentum $q_\pi(p)$ arises from $D^{*+} \rightarrow D^0\pi^+$ vertex, and can be determined kinematically [18]. The second term of the integrand with \bar{p} comes from symmetrizing the $D^0D^0\pi^+$ amplitude due to two identical D^0 s in the final state. With \mathcal{N} being an overall normalization factor, the shape of $D^0D^0\pi^+$ mass spectrum does not depend on any free parameters. In order to compare with the LHCb data, an energy resolution function given in Ref. [10] is convolved with Eq. (7).

Shown in Fig. 4 by the black and red bands are our theoretical calculations for $D^0D^0\pi^+$ mass spectrum obtained from $V_{\text{fit}}^B(r; m_\pi)$ with $m_\pi = 146.4$ MeV and $m_\pi = 135.0$ MeV, respectively. In both cases, experimental values for m_{D^{*+}, D^0, π^+} [58] are adopted in the kinematics in order to keep the same phase space with the experiment. Shown together by the black points are LHCb data [10]. The obtained mass spectrum has a pronounced peak around the $D^{*+}D^0$ threshold, and the peak position shifts to the left as m_π decreases; this is consistent with the evolution from a near-threshold virtual pole to a loosely bound pole. At the physical pion mass, the red band with a peak just on the $D^{*+}D^0$ threshold provides a better description of the LHCb data, though visible differences still exist. This calls for a direct calculation of the potential with the physical quark masses as well as with the isospin-breaking effect.

Summary and discussion.— In this Letter, we present an investigation on the scattering properties of the D^*D system based on the $(2+1)$ -flavor lattice QCD simulations with nearly physical pion mass $m_\pi = 146$ MeV. The attractive potential between D^* and D in the $I = 0$ and S -wave channel is extracted from hadronic spacetime correlation. The long-range part of the potential is found to be dominated by the two-pion exchange at least in the

range $1 < r < 2$ fm. The overall attraction is found to be strong enough to lead a near-threshold virtual state with a pole position $E_{\text{pole}} = -59 \begin{pmatrix} +53 \\ -99 \end{pmatrix} \begin{pmatrix} +2 \\ -67 \end{pmatrix}$ keV and a large scattering length $1/a_0 = 0.05(5) \begin{pmatrix} +2 \\ -2 \end{pmatrix}$ fm $^{-1}$. The virtual state is shown to evolve into a loosely bound state at the physical point by using a potential modified to $m_\pi = 135$ MeV based on the TPE. Such a potential can also provide a semiquantitative description to the $D^0D^0\pi^+$ mass spectrum measured by LHCb Collaboration.

We are currently under way to perform physical-point simulations in $(2+1)$ -flavor QCD. It is also important in the future to study the OPE and the associated left-hand cut as well as to perform high-precision study with the isospin-breaking effect and open three-body-channel effect by $(1+1+1)$ -flavor or $(1+1+1+1)$ -flavor lattice QCD + QED calculations with the physical quark masses.

Acknowledgments.— We thank members of the HAL QCD Collaboration for stimulating discussions. Y.L. thanks Meng-Lin Du, and Xu Feng for the helpful discussions. We thank members of the PACS Collaboration for the gauge configuration generation conducted on the K computer at RIKEN. The lattice QCD measurements have been performed on Fugaku and HOKUSAI supercomputers at RIKEN. We thank ILDG/JLDG [60], which serves as essential infrastructure in this study. This work was partially supported by HPCI System Research Project (hp120281, hp130023, hp140209, hp150223, hp150262, hp160211, hp170230, hp170170, hp180117, hp190103, hp200130, hp210165, hp210212, hp220240, hp220066, and hp220174), the National Key R&D Program of China (Contracts No. 2017YFE0116700 and No. 2018YFA0404400), the National Natural Science Foundation of China (Grants No. 11935003, No. 11975031, No. 11875075, No. 12070131001, and No. 12141501), the JSPS (Grants No. JP18H05236, No. JP22H00129, No. JP19K03879, No. JP18H05407, No. JP21K03555, and No. JP23H05439), “Priority Issue on Post-K computer” (Elucidation of the Fundamental Laws and Evolution of the Universe), “Program for Promoting Researches on the Supercomputer Fugaku” (Simulation for basic science: from fundamental laws of particles to creation of nuclei) and (Simulation for basic science: approaching the new quantum era), and Joint Institute for Computational Fundamental Science (JICFuS).

* helvetia@pku.edu.cn

† saoki@yukawa.kyoto-u.ac.jp

‡ doi@ribf.riken.jp

§ thatsuda@riken.jp

¶ yikeda@cider.osaka-u.ac.jp

** mengj@pku.edu.cn

[1] H.-X. Chen, W. Chen, X. Liu, and S.-L. Zhu, Phys.

- Rept. **639**, 1 (2016), arXiv:1601.02092 [hep-ph].
- [2] A. Esposito, A. Pilloni, and A. D. Polosa, Phys. Rept. **668**, 1 (2017), arXiv:1611.07920 [hep-ph].
- [3] R. F. Lebed, R. E. Mitchell, and E. S. Swanson, Prog. Part. Nucl. Phys. **93**, 143 (2017), arXiv:1610.04528 [hep-ph].
- [4] A. Ali, J. S. Lange, and S. Stone, Prog. Part. Nucl. Phys. **97**, 123 (2017), arXiv:1706.00610 [hep-ph].
- [5] F.-K. Guo, C. Hanhart, U.-G. Meißner, Q. Wang, Q. Zhao, and B.-S. Zou, Rev. Mod. Phys. **90**, 015004 (2018), [Erratum: Rev.Mod.Phys. 94, 029901 (2022)], arXiv:1705.00141 [hep-ph].
- [6] Y. Yamaguchi, A. Hosaka, S. Takeuchi, and M. Takizawa, J. Phys. G **47**, 053001 (2020), arXiv:1908.08790 [hep-ph].
- [7] S. L. Olsen, T. Skwarnicki, and D. Zieminska, Rev. Mod. Phys. **90**, 015003 (2018), arXiv:1708.04012 [hep-ph].
- [8] N. Brambilla, S. Eidelman, C. Hanhart, A. Nefediev, C.-P. Shen, C. E. Thomas, A. Vairo, and C.-Z. Yuan, Phys. Rept. **873**, 1 (2020), arXiv:1907.07583 [hep-ex].
- [9] R. Aaij *et al.* (LHCb), Nature Phys. **18**, 751 (2022), arXiv:2109.01038 [hep-ex].
- [10] R. Aaij *et al.* (LHCb), Nature Commun. **13**, 3351 (2022), arXiv:2109.01056 [hep-ex].
- [11] J. P. Ader, J. M. Richard, and P. Taxil, Phys. Rev. D **25**, 2370 (1982).
- [12] H. J. Lipkin, Phys. Lett. B **172**, 242 (1986).
- [13] S. Zouzou, B. Silvestre-Brac, C. Gignoux, and J. M. Richard, Z. Phys. C **30**, 457 (1986).
- [14] D. Janc and M. Rosina, Few Body Syst. **35**, 175 (2004), arXiv:hep-ph/0405208.
- [15] D. Ebert, R. N. Faustov, V. O. Galkin, and W. Lucha, Phys. Rev. D **76**, 114015 (2007), arXiv:0706.3853 [hep-ph].
- [16] A. Esposito, M. Papinutto, A. Pilloni, A. D. Polosa, and N. Tantalo, Phys. Rev. D **88**, 054029 (2013), arXiv:1307.2873 [hep-ph].
- [17] M. Karliner and J. L. Rosner, Phys. Rev. Lett. **119**, 202001 (2017), arXiv:1707.07666 [hep-ph].
- [18] M.-L. Du, V. Baru, X.-K. Dong, A. Filin, F.-K. Guo, C. Hanhart, A. Nefediev, J. Nieves, and Q. Wang, Phys. Rev. D **105**, 014024 (2022), arXiv:2110.13765 [hep-ph].
- [19] X.-Z. Ling, M.-Z. Liu, L.-S. Geng, E. Wang, and J.-J. Xie, Phys. Lett. B **826**, 136897 (2022), arXiv:2108.00947 [hep-ph].
- [20] Y. Kim, M. Oka, and K. Suzuki, Phys. Rev. D **105**, 074021 (2022), arXiv:2202.06520 [hep-ph].
- [21] S. S. Agaev, K. Azizi, and H. Sundu, JHEP **06**, 057 (2022), arXiv:2201.02788 [hep-ph].
- [22] H.-X. Chen, W. Chen, X. Liu, Y.-R. Liu, and S.-L. Zhu, Rept. Prog. Phys. **86**, 026201 (2023), arXiv:2204.02649 [hep-ph].
- [23] Y. Ikeda, B. Charron, S. Aoki, T. Doi, T. Hatsuda, T. Inoue, N. Ishii, K. Murano, H. Nemura, and K. Sasaki, Phys. Lett. B **729**, 85 (2014), arXiv:1311.6214 [hep-lat].
- [24] S. Chen, C. Shi, Y. Chen, M. Gong, Z. Liu, W. Sun, and R. Zhang, Phys. Lett. B **833**, 137391 (2022), arXiv:2206.06185 [hep-lat].
- [25] M. Padmanath and S. Prelovsek, Phys. Rev. Lett. **129**, 032002 (2022), arXiv:2202.10110 [hep-lat].
- [26] G. K. C. Cheung, C. E. Thomas, J. J. Dudek, and R. G. Edwards (Hadron Spectrum), JHEP **11**, 033 (2017), arXiv:1709.01417 [hep-lat].
- [27] P. Junnarkar, N. Mathur, and M. Padmanath, Phys. Rev. D **99**, 034507 (2019), arXiv:1810.12285 [hep-lat].
- [28] N. Ishii, S. Aoki, and T. Hatsuda, Phys. Rev. Lett. **99**, 022001 (2007).
- [29] N. Ishii, S. Aoki, T. Doi, T. Hatsuda, Y. Ikeda, T. Inoue, K. Murano, H. Nemura, and K. Sasaki (HAL QCD Collaboration), Physics Letters B **712**, 437 (2012).
- [30] S. Aoki and T. Doi, Frontiers in Physics **8**, 307 (2020).
- [31] T. Miyamoto, Y. Akahoshi, S. Aoki, T. Aoyama, T. Doi, S. Gongyo, and K. Sasaki, Phys. Rev. D **101**, 074514 (2020).
- [32] Supplemental Material at [URL].
- [33] S. Aoki, N. Ishii, T. Doi, T. Hatsuda, Y. Ikeda, T. Inoue, K. Murano, H. Nemura, and K. Sasaki (HAL QCD), Proc. Japan Acad. B **87**, 509 (2011), arXiv:1106.2281 [hep-lat].
- [34] T. Iritani, S. Aoki, T. Doi, T. Hatsuda, Y. Ikeda, T. Inoue, N. Ishii, H. Nemura, and K. Sasaki (HAL QCD Collaboration), JHEP **03**, 007 (2019), arXiv:1812.08539 [hep-lat].
- [35] Y. Lyu, H. Tong, T. Sugiura, S. Aoki, T. Doi, T. Hatsuda, J. Meng, and T. Miyamoto, Phys. Rev. D **105**, 074512 (2022).
- [36] K.-I. Ishikawa, N. Ishizuka, Y. Kuramashi, Y. Nakamura, Y. Namekawa, Y. Taniguchi, N. Ukita, T. Yamazaki, and T. Yoshie (PACS Collaboration), Proc. Sci. LATTICE2015, 075 (2016), arXiv:1511.09222 [hep-lat].
- [37] S. Aoki, Y. Kuramashi, and S.-i. Tominaga, Prog. Theor. Phys. **109**, 383 (2003), arXiv:hep-lat/0107009.
- [38] Y. Namekawa (PACS Collaboration), Proc. Sci. LATTICE2016, 125 (2017).
- [39] Y. Lyu, T. Doi, T. Hatsuda, Y. Ikeda, J. Meng, K. Sasaki, and T. Sugiura, Phys. Rev. D **106**, 074507 (2022), arXiv:2205.10544 [hep-lat].
- [40] K.-I. Ishikawa, I. Kanamori, H. Matsufuru, I. Miyoshi, Y. Mukai, Y. Nakamura, K. Nitadori, and M. Tsuji, Comput. Phys. Commun. **282**, 108510 (2023), arXiv:2109.10687 [hep-lat].
- [41] http://bridge.kek.jp/Lattice-code/index_e.html.
- [42] T. Doi and M. G. Endres, Comput. Phys. Commun. **184**, 117 (2013), arXiv:1205.0585 [hep-lat].
- [43] S. Cali, F. Knechtli, and T. Korzec, Eur. Phys. J. C **79**, 607 (2019), arXiv:1905.12971 [hep-lat].
- [44] R. L. Jaffe and F. Wilczek, Phys. Rev. Lett. **91**, 232003 (2003), arXiv:hep-ph/0307341.
- [45] A. Selem and F. Wilczek, in *Ringberg Workshop on New Trends in HERA Physics 2005* (2006) pp. 337–356, arXiv:hep-ph/0602128.
- [46] S. H. Lee and S. Yasui, Eur. Phys. J. C **64**, 283 (2009), arXiv:0901.2977 [hep-ph].
- [47] C.-R. Deng and S.-L. Zhu, Sci. Bull. **67**, 1522 (2022), arXiv:2204.11079 [hep-ph].
- [48] S. Noh, W. Park, and S. H. Lee, Phys. Rev. D **103**, 114009 (2021), arXiv:2102.09614 [hep-ph].
- [49] O. Andreev, Phys. Rev. D **105**, 086025 (2022), arXiv:2111.14418 [hep-ph].
- [50] S. Aoki and T. Aoki, in *39th International Symposium on Lattice Field Theory* (2022) arXiv:2212.00202 [hep-lat].
- [51] P. Bicudo, K. Cichy, A. Peters, and M. Wagner, Phys. Rev. D **93**, 034501 (2016), arXiv:1510.03441 [hep-lat].
- [52] S. Ohkoda, Y. Yamaguchi, S. Yasui, K. Sudoh, and A. Hosaka, Phys. Rev. D **86**, 034019 (2012), arXiv:1202.0760 [hep-ph].
- [53] N. Li, Z.-F. Sun, X. Liu, and S.-L. Zhu, Phys. Rev. D **88**, 114008 (2013), arXiv:1211.5007 [hep-ph].

- [54] T. Inoue, S. Aoki, T. Doi, T. Hatsuda, Y. Ikeda, N. Ishii, K. Murano, H. Nemura, and K. Sasaki (HAL QCD), Nucl. Phys. A **881**, 28 (2012), arXiv:1112.5926 [hep-lat].
- [55] B. Hörz *et al.*, Phys. Rev. C **103**, 014003 (2021), arXiv:2009.11825 [hep-lat].
- [56] S. Amarasinghe, R. Baghdadi, Z. Davoudi, W. Detmold, M. Illa, A. Parreno, A. V. Pochinsky, P. E. Shanahan, and M. L. Wagman, (2021), arXiv:2108.10835 [hep-lat].
- [57] Y. Aoki *et al.* (Flavour Lattice Averaging Group (FLAG)), Eur. Phys. J. C **82**, 869 (2022), arXiv:2111.09849 [hep-lat].
- [58] P. A. Zyla *et al.* (Particle Data Group), Progress of Theoretical and Experimental Physics **2020** (2020), 083C01.
- [59] M. Albaladejo, Phys. Lett. B **829**, 137052 (2022), arXiv:2110.02944 [hep-ph].
- [60] <http://www.lqcd.org/ildg> and <http://www.jldg.org>.

SUPPLEMENTAL MATERIAL

We present the S - and D -wave components of $R(\mathbf{r}, t)$, the effective mass of $D^{(*)}$, a detailed analysis of the potential, the distribution of E_{pole} , and a chiral extrapolation of the inverse of scattering length ($1/a_0$) in this supplemental material.

The S - and D -wave components of $R(\mathbf{r}, t)$

We show the S - and D -wave components of $R(\mathbf{r}, t)$ in Fig. S1. The D -wave component is around three order-of-magnitude smaller than the S -wave component, and is consistent with zero within the statistical error.

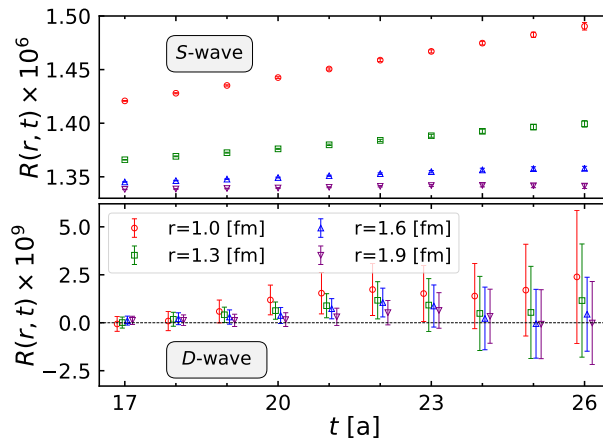


FIG. S1. The S - (upper) and D - (lower) wave components of $R(\mathbf{r}, t)$ as a function of t for several values of r where two-pion-exchange (TPE) is relevant.

The effective mass

The effective masses for D^* and D , defined as $m_{\text{eff}}(t) = \ln \frac{C(t)}{C(t+1)}$ with $C(t)$ being the two-piont function, are shown in Fig. S2.

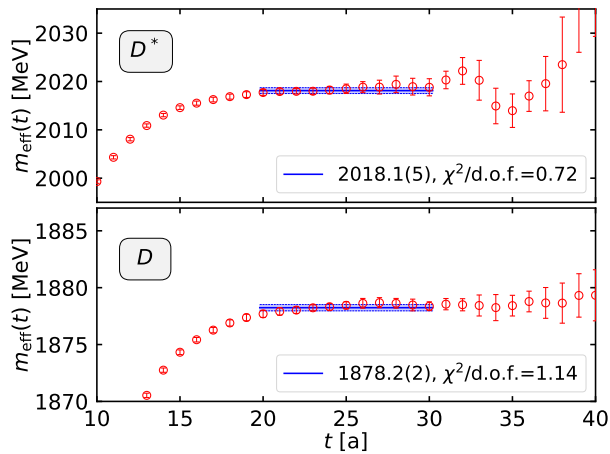


FIG. S2. The effective mass for D^* (upper) and D (lower). The blue bands show the results of correlated single-state fit.

A detailed analysis of the potential

In Fig. S3, we show the long-range potential up to $r = 4$ fm (half of the box size) together with two fits as bands.

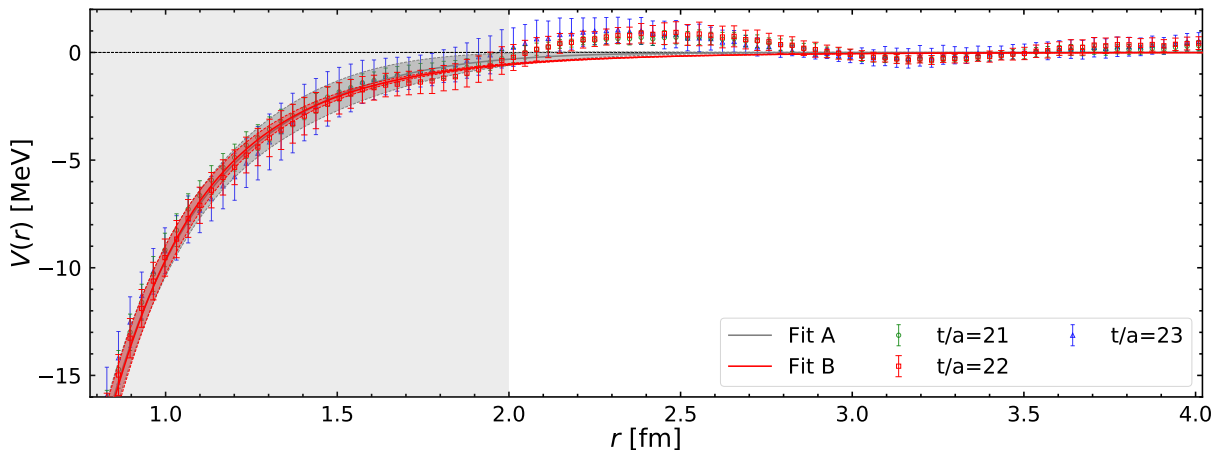


FIG. S3. The D^*D potential $V(r)$ in the $I = 0$ and S -wave channel at Euclidean time $t/a = 21$ (green circles), 22 (red squares), and 23 (blue triangles). The gray (red) band shows the fitted potential with V_{fit}^A (V_{fit}^B) for $t/a = 22$. Fit range is $0 < r < 2$ fm.

We show in Fig. S4 the spatial effective energy defined as,

$$E_{\text{eff}}(r) = -\frac{\ln[V(r)r^2/a_3]}{r}, \quad (\text{S1})$$

which has a plateau at $2m_\pi = 292.8$ MeV for $r > 1.0$ fm. This numerically shows that the long-range potential is consistent with the TPE form $\sim \frac{e^{-2m_\pi r}}{r^2}$.

The normalized covariance matrix, defined as $\frac{\text{Cov}(x,y)}{\sigma_x \sigma_y}$ with $\text{Cov}(x,y)$ being the covariance between x and y and

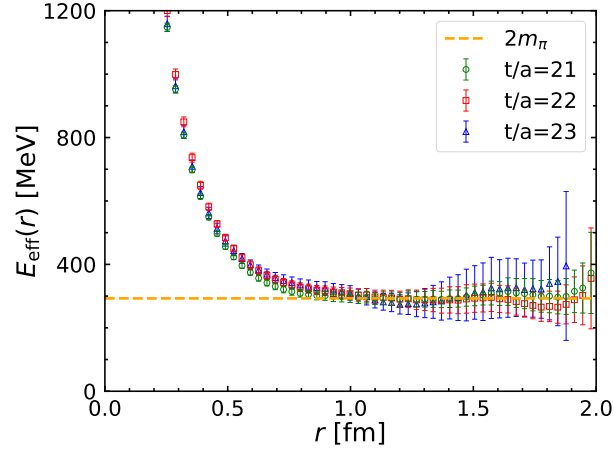


FIG. S4. The spatial effective energy $E_{\text{eff}}(r)$ as a function of separation r at Euclidean time $t/a = 21$ (green circles), 22 (red squares), and 23 (blue triangles). The orange dashed line denotes $2m_\pi$ with $m_\pi = 146.4$ MeV.

$\sigma_{x(y)}$ being the standard error of $x(y)$, of the fitted parameters $(a_1, b_1, \dots, a_4, b_4)$ in V_{fit}^A are

$$\begin{bmatrix} 1.00 & -0.58 & 0.43 & -0.80 & -0.40 & -0.28 & -0.10 & 0.07 \\ & 1.00 & -0.39 & 0.77 & 0.76 & 0.54 & 0.12 & -0.08 \\ & & 1.00 & -0.66 & -0.08 & -0.79 & -0.68 & -0.64 \\ & & & 1.00 & 0.48 & 0.68 & 0.43 & 0.23 \\ & & & & 1.00 & 0.03 & -0.46 & -0.59 \\ & & & & & 1.00 & 0.85 & 0.69 \\ & & & & & & 1.00 & 0.93 \\ & & & & & & & 1.00 \end{bmatrix}, \quad (\text{S2})$$

and $(a_1, b_1, \dots, a_3, b_3)$ in V_{fit}^B are

$$\begin{bmatrix} 1.00 & -0.49 & -0.03 & -0.63 & 0.09 & -0.18 \\ & 1.00 & 0.68 & 0.66 & 0.21 & 0.53 \\ & & 1.00 & 0.14 & -0.29 & -0.03 \\ & & & 1.00 & 0.36 & 0.81 \\ & & & & 1.00 & 0.80 \\ & & & & & 1.00 \end{bmatrix}. \quad (\text{S3})$$

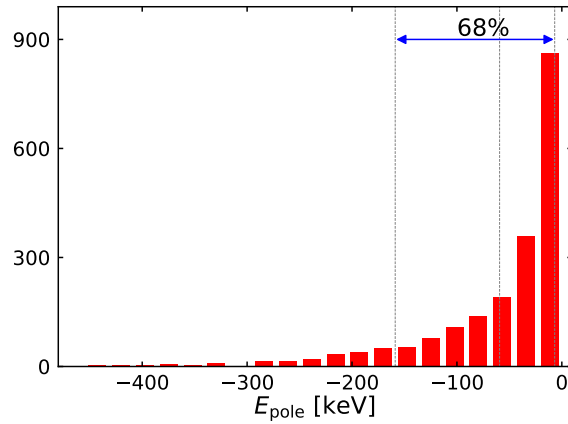


FIG. S5. The histogram of the PDF of E_{pole} . $\mu - a$, μ , and $\mu + b$ are also shown as dashed lines.

The distribution of E_{pole}

E_{pole} is defined as $E_{\text{pole}} = \sqrt{m_{D^*}^2 - \kappa_{\text{pole}}^2} + \sqrt{m_D^2 - \kappa_{\text{pole}}^2} - (m_{D^*} + m_D)$ and is less than or equal to zero. The probability distribution function (PDF) of E_{pole} from our lattice simulations is shown in Fig. S5. For such an asymmetric distribution, we define the statistical error by demanding $P(\mu - a < E_{\text{pole}} < \mu + b) = 68\%$, $P(E_{\text{pole}} < \mu - a) = 32\% \times P(E_{\text{pole}} < \mu)$ and $P(E_{\text{pole}} > \mu + b) = 32\% \times P(E_{\text{pole}} > \mu)$ with μ and a (b) being the mean value and the lower (upper) bound. Then, $E_{\text{pole}} = \mu \left(\begin{smallmatrix} +b \\ -a \end{smallmatrix} \right) = -59 \left(\begin{smallmatrix} +53 \\ -99 \end{smallmatrix} \right)$ keV is quoted.

A chiral extrapolation of $1/a_0$

TABLE S1. The fit parameters in Eq. (S4) with 1σ uncertainty quoted in the parenthesis. The corresponding value for $1/a_0$ at $m_\pi = 135.0$ MeV is shown in the last column.

c [fm^{-1}]	d	$\chi^2/\text{d.o.f.}$	$1/a_0$ [fm^{-1}]
-0.33(6)	18(1) $\text{GeV}^{-2} \cdot \text{fm}^{-1}$	0.1	-0.01(9)

Shown in Fig. S6 is a chiral extrapolation of lattice data for $1/a_0$ based on following fit function,

$$1/a_0(m_\pi) = c + dm_\pi^2. \quad (\text{S4})$$

Fit parameters c and d together with corresponding $1/a_0$ for $m_\pi = 135.0$ MeV are shown in Table S1. Result for $1/a_0$ from fit function agrees with the value of $1/a_0 = -0.03(4) \text{ fm}^{-1}$ from the potential modified to the same pion mass according to the TPE, which indicates that the modification of the potential is reasonable.

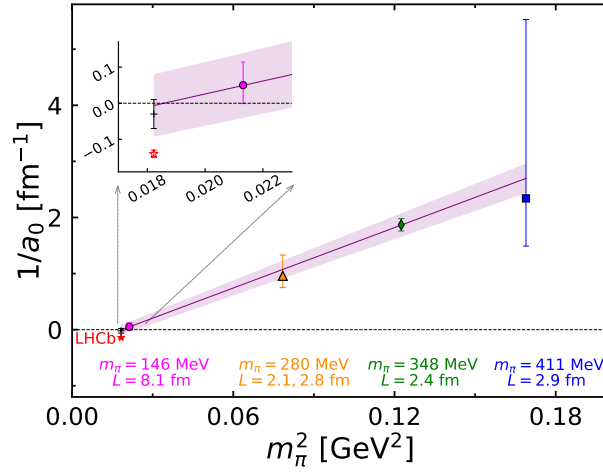


FIG. S6. The chiral extrapolation of lattice data for $1/a_0$ based on fit function in Eq. (S4). The black plus symbol shows the value from the potential modified to $m_\pi = 135$ MeV.